Consistency Models for Scalable and Fast Simulation-Based Inference

Marvin Schmitt *1 Valentin Pratz *23 Ullrich Köthe 2 Paul-Christian Bürkner 4 Stefan T. Radev 5

Abstract

Simulation-based inference (SBI) is constantly in search of more expressive algorithms for accurately inferring the parameters of complex models from noisy data. We present consistency models for neural posterior estimation (CMPE), a new free-form conditional sampler for scalable, fast, and amortized SBI with generative neural networks. CMPE combines the advantages of normalizing flows and flow matching methods into a single generative architecture: It essentially distills a continuous probability flow and enables rapid few-shot inference with an unconstrained architecture that can be tailored to the structure of the estimation problem. Our empirical evaluation demonstrates that CMPE not only outperforms current state-of-the-art algorithms on three hard low-dimensional problems, but also achieves competitive performance in a high-dimensional Bayesian denoising experiment and in estimating a computationally demanding multi-scale model of tumor spheroid growth.

1. Introduction

Computer simulations play a fundamental role across countless scientific disciplines, ranging from physics to biology, and from climate science to economics (Lavin et al., 2021). Simulation programs can generate observables $\mathbf{x} \in \mathcal{X}$ as a function of unknown parameters $\boldsymbol{\theta} \in \boldsymbol{\Theta}$ and latent program states $\boldsymbol{\xi} \in \Xi$ (Cranmer et al., 2020). This forward problem is typically well-understood through scientific theories instantiated as generative models.

The inverse problem, however, is much harder, and forms the crux of Bayesian (probabilistic) inference: Reasoning about the unknowns θ based on observables x. Bayes' theorem captures the full *posterior distribution* of plausible parameters θ conditional on the observed data x as

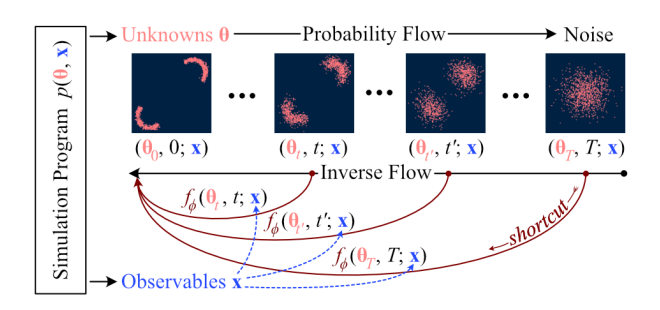


Figure 1: Inverting a probability flow on a target vector $\boldsymbol{\theta}$ forms the core of modern denoising models. Consistency models (Song et al., 2023) learn a shortcut f_{ϕ} that maps any point on the trajectory directly to the origin $\boldsymbol{\theta}_0$. We extend consistency models by conditioning on observable data \mathbf{x} and infer mechanistic model parameters $\boldsymbol{\theta}$ as the target vector. As a consequence, the probability distribution over the origin $p(\boldsymbol{\theta}_0 \mid \mathbf{x})$ is the Bayesian posterior by definition. We call this approach consistency model posterior estimation (CMPE), which is a new amortized method for scalable and fast simulation-based inference.

 $p(\theta \mid \mathbf{x}) \propto p(\theta) p(\mathbf{x} \mid \theta)$, given a prior $p(\theta)$. While generating synthetic data from the simulation program is possible (albeit potentially slow), the likelihood density $p(\mathbf{x} \mid \theta)$ is generally not explicitly available. Instead, it is only implicitly defined through a high-dimensional integral over all possible program execution paths (Cranmer et al., 2020). A new era of simulation intelligence (Lavin et al., 2021) addresses this challenging setting with remarkable success across application domains (Butter et al., 2022; Radev et al., 2021b; Shiono, 2021; Bieringer et al., 2021; von Krause et al., 2022; Ghaderi-Kangavari et al., 2023).

These advances in *simulation-based inference* (SBI) are codeveloping with rapid progress in conditional generative modeling. Currently, advancements in generative neural networks primarily manifest in remarkable performance on generating images (Goodfellow et al., 2014), videos (Vondrick et al., 2016), and audio (Engel et al., 2020). Within the class of generative models, score-based diffusion models (Song et al., 2021; Rombach et al., 2022; Ho et al., 2020; Batzolis et al., 2021) have recently attracted significant attention due to their sublime performance as realistic generators. Diffusion models are strikingly flexible but re-

^{*}Equal contribution ¹University of Stuttgart ²Heidelberg University ³ELIZA ⁴TU Dortmund University ⁵Rensselaer Polytechnic Institute. Correspondence to: Marvin Schmitt <mail.marvinschmitt@gmail.com>.

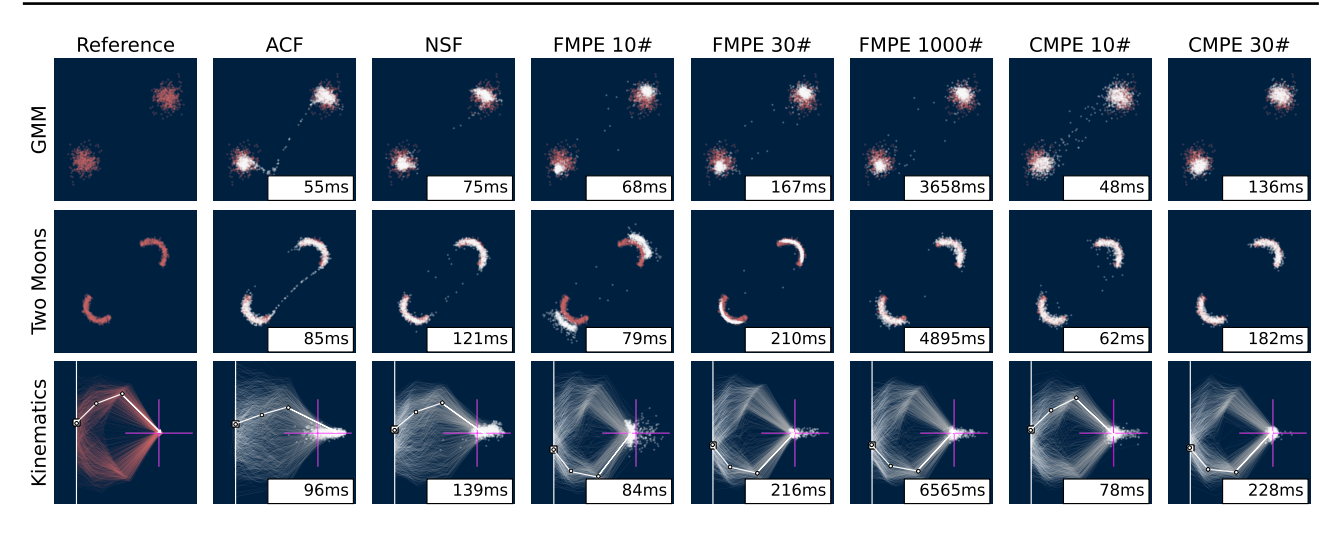


Figure 2: Experiments 1–3. 1000 posterior draws for one unseen test instance per task, as well as sampling time in milliseconds. All amortized neural approximators were trained with a small budget of M=1024 simulations. The bottom row shows the posterior predictive distribution in the kinematics task, and the pink cross-hair indicates the true end location \mathbf{x} of the robot arm. Across all benchmarks, CMPE (Ours) yields the best trade-off between fast sampling speed and high accuracy. ACF: affine coupling flow, NSF: neural spline flow, FMPE: flow matching posterior estimation, CMPE: consistency model posterior estimation (Ours), K# denotes K sampling steps during inference.

quire a multi-step sampling phase to denoise samples (Song et al., 2021). To address this shortcoming, Song et al. (2023) proposed *consistency models*, which are trained to perform few-step generation *by design*. In this paper, we port consistency models to simulation-based inference (see Figure 1) to achieve an unprecedented combination of both *scalable and fast* neural posterior estimation. Our contributions are:

- We adapt consistency models to simulation-based Bayesian inference and propose consistency model posterior estimation (CMPE);
- 2. We illustrate the fundamental advantages of consistency models for simulation-based inference: expressive free-form architectures *and* fast inference;
- 3. We demonstrate that CMPE outperforms both normalizing flows and flow matching on three benchmark experiments (see Figure 2 above), high-dimensional Bayesian denoising, and a tumor spheroid model.

2. Preliminaries and Related Work

This section recaps simulation-based inference via normalizing flows, flow matching, and score-based diffusion models.

2.1. Simulation-Based Inference (SBI)

The defining property of SBI methods is that they rely only on the ability to sample from the data-generating process, $p(\mathbf{x}, \boldsymbol{\theta})$, as opposed to likelihood-based methods which rely on the ability to evaluate the likelihood $p(\mathbf{x} | \boldsymbol{\theta})$. Closely

related, probabilistic neural methods for SBI can be classified into *sequential* (Papamakarios & Murray, 2016; Lueckmann et al., 2017; Greenberg et al., 2019; Durkan et al., 2020; Deistler et al., 2022; Sharrock et al., 2022) vs. *amortized* (Ardizzone et al., 2019; Gonçalves et al., 2020; Radev et al., 2020; Pacchiardi & Dutta, 2022; Avecilla et al., 2022; Dax et al., 2023b; Geffner et al., 2022; Radev et al., 2021a; Elsemüller et al., 2023b) methods.

Sequential inference algorithms iteratively refine the prior $p(\theta)$ to generate simulations in the vicinity of the target observation. Thus, they are not amortized, as each new observed data set requires a costly re-training of the neural approximator tailored to the particular target observation. In contrast, amortized methods train the neural approximator to generalize over the entire prior predictive space of the model. This allows us to query the approximator with any new data set that is presumed to originate from the model's scope. In fact, amortization can be performed across any component of the model, including multiple data sets (Gonçalves et al., 2020) and contextual factors, such as the number of observations in a data set (Radev et al., 2020), heterogeneous data sources (Schmitt et al., 2023b), or even different probabilistic models and data configurations (Elsemüller et al., 2023a). Our current work is situated in the amortized setting.

2.2. Normalizing Flows for Neural Posterior Estimation

Neural posterior estimation (NPE) methods for SBI have traditionally relied on conditional normalizing flows for

Table 1: Comparison of neural posterior estimation methods, adapted from Dax et al. (2023b). NPE: neural posterior estimation; NPSE: neural posterior score estimation; FMPE: flow matching posterior estimation; CMPE: consistency model posterior estimation (Ours).

	NPE	NPSE	FMPE	CMPE (Ours)
Tractable posterior density	Yes	No	Yes	Partially ¹
Unconstrained networks	No	Yes	Yes	Yes
Network passes for sampling	Single	Many	Many	Few

¹See Section 3.4 for details.

learning a neural density estimator $p_{\phi}(\theta \mid \mathbf{x})$ from simulated pairs (θ, \mathbf{x}) of parameters and data (Rezende & Mohamed, 2015; Papamakarios et al., 2021). The learnable neural network weights are subsumed as ϕ . A normalizing flow defines a *single-shot* transformation between the parameters θ and a latent variable \mathbf{z} with a simple base distribution (e.g., Gaussian). Normalizing flows can learn closed-form approximate densities via maximum likelihood training:

$$\mathcal{L}_{\text{NPE}} = \mathbb{E}_{p(\boldsymbol{\theta}, \mathbf{x})}[-\log p_{\boldsymbol{\phi}}(\boldsymbol{\theta} \,|\, \mathbf{x})] \tag{1}$$

Two prominent normalizing flow architectures in SBI are affine coupling flows (ACF; Dinh et al., 2016) and neural spline flows (NSF; Durkan et al., 2019). A major disadvantage of these architectures is the invertibility requirement: It restricts the design space of the neural networks to invertible functions with cheap Jacobian calculations. In the following, we will briefly recap recent works that have pioneered the use of *multi-step*, *free-form* architectures for SBI, inspired by the success of such models in a variety of generative tasks (Batzolis et al., 2021; Rombach et al., 2022).

2.3. Flow Matching for Posterior Estimation

Dax et al. (2023b) applied flow matching techniques (Lipman et al., 2023; Liu et al., 2022) in SBI, an approach called flow matching posterior estimation (FMPE). Flow matching lifts the invertibility restrictions and enables the use of freeform neural networks. FMPE is based on optimal transport, where the mapping between base and target distribution is parameterized by a continuous process driven by a vector field on the sample space for each time step $t \in [0,1]$. Here, the distribution at t=1 is a unit Gaussian $\mathcal{N}(\mathbf{0},\mathbf{I})$ and the distribution at t=0 is the target posterior. The FMPE loss replaces the maximum likelihood term in the NPE objective (Eq. 1) with a conditional flow matching objective,

$$\mathcal{L}_{\text{FMPE}} = \mathbb{E}_{p(\mathbf{x}, \boldsymbol{\theta})} \left[\int_{0}^{1} \| u_{t}(\boldsymbol{\theta}_{t} | \boldsymbol{\theta}) - \mu_{\boldsymbol{\phi}}(\boldsymbol{\theta}_{t}, t; \mathbf{x}) \|^{2} dt \right],$$
(2)

where μ_{ϕ} denotes the conditional vector field parameterized by a free-form neural network with trainable parameters ϕ , and u_t denotes a marginal vector field, which can be as simple as $u_t(\theta_t | \theta) = \theta_1 - \theta$ for all t (Liu et al., 2022). We obtain posterior draws $\theta_0 \sim p(\theta \mid \mathbf{x})$ by solving $\mathrm{d}\theta_t = -\mu(\theta_t, t; \mathbf{x})$ in reverse on $t \in [0, 1]$, starting with noise samples $\theta_1 \sim \mathcal{N}(\mathbf{0}, \mathbf{I})$. We can use any off-the-shelf ODE solver for transforming noise θ_1 into a draw θ_0 from the approximate posterior. In principle, the number of steps K in the ODE solver can be adjusted by setting the step size $\mathrm{d}t = 1/K$. This increases the sampling speed, but FMPE is not designed to optimize few-step sampling performance. We confirm this in our experiments with a rectified flow that encourages straight-path solutions (Liu et al., 2022).

2.4. Neural Posterior Score Estimation

Another approach to simulation-based inference with free-form networks lies in neural posterior score estimation (NPSE). This direction uses conditional score-based diffusion models (Song & Ermon, 2019; Song et al., 2021) to learn the posterior distribution. Sharrock et al. (2022) propose sequential NPSE, which trains a score-based diffusion model in a sequential (non-amortized) manner. With a slightly different focus, (Geffner et al., 2022) factorize the posterior distribution and learn scores of the (diffused) posterior for subsets (down to a single observation) of a larger data set. Subsequently, the information from the subsets is aggregated by combining the learned scores to approximate the posterior distribution of the entire data set.

Crucially, both methods rely on the basic formulation of score-based diffusion models: They gradually diffuse the target distribution through a diffusion process $\{\theta_t\}_{t\in[0,T]}$ via a stochastic differential equation,

$$d\theta_t = \mu(\theta_t, t; \mathbf{x})dt + \sigma(t)d\mathbf{w}_t, \tag{3}$$

with drift coefficient μ , diffusion coefficient σ , time $t \in [0,T]$, and Brownian motion $\{\mathbf w_t\}_{t\in [0,T]}$. At each time t, the current (diffused) distribution of $\boldsymbol \theta$ conditional on $\mathbf x$ is denoted as $p_t(\boldsymbol \theta \mid \mathbf x)$. Crucially, the distribution at t=0 equals the target posterior distribution, $p_0(\boldsymbol \theta \mid \mathbf x) \equiv p(\boldsymbol \theta \mid \mathbf x)$, and the distribution at t=T is pure noise (see below). Song et al. (2021) prove that there exists an ordinary differential equation ("Probability Flow ODE") whose solution trajectories at time t are distributed according to $p_t(\boldsymbol \theta \mid \mathbf x)$:

$$d\theta_t = \left[\mu(\theta_t, t; \mathbf{x}) - \frac{1}{2} \sigma(t)^2 \nabla \log p_t(\theta_t \mid \mathbf{x}) \right] dt, \quad (4)$$

where $\nabla \log p_t(\boldsymbol{\theta}_t \,|\, \mathbf{x})$ is the score function of $p_t(\boldsymbol{\theta} \,|\, \mathbf{x})$. This differential equation is usually designed to yield a spherical Gaussian noise distribution $p_T(\boldsymbol{\theta} \,|\, \mathbf{x}) \approx \mathcal{N}(\mathbf{0}, T^2\mathbf{I})$ after the diffusion process. Since we do not have access to the target posterior $p(\boldsymbol{\theta} \,|\, \mathbf{x})$, score-based diffusion models train a time-dependent score network $s_{\boldsymbol{\phi}}(\boldsymbol{\theta}_t, t, \mathbf{x}) \approx \nabla \log p_t(\boldsymbol{\theta}_t \,|\, \mathbf{x})$ via score matching and insert it into Eq. 4. Setting $\mu(\boldsymbol{\theta}_t, t;\, \mathbf{x}) = 0$ and $\sigma_t = \sqrt{2t}$, the estimate of the Probability Flow ODE becomes $\mathrm{d}\boldsymbol{\theta}_t = -ts_{\boldsymbol{\phi}}(\boldsymbol{\theta}_t, \mathbf{x}, t)\mathrm{d}t$

(Karras et al., 2022). Finally, we can generate a random draw from the noise distribution $\theta_T \sim \mathcal{N}(\mathbf{0}, T^2\mathbf{I})$ and solve the Probability Flow ODE backwards for a trajectory $\{\theta_t\}_{t\in[T,0]}$. The end of the trajectory θ_0 represents a draw from the approximate posterior $p_0(\theta_0 \mid \mathbf{x}) \approx p(\theta \mid \mathbf{x})$.

Numerical stability The solver is usually stopped at a fixed small positive number $t = \varepsilon$ to prevent numerical instabilities (Song et al., 2023), so we use θ_{ε} to denote the draw from the approximate posterior. For simplicity, we will also refer to θ_{ε} as the *trajectory's origin*.

3. Consistency Model Posterior Estimation

Diffusion models have one crucial drawback: At inference time, they require solving many differential equations which slows down their sampling speed. This is particularly troublesome in SBI applications, which typically require thousands of samples for thousands of data sets. Consistency models (Song et al., 2023) address this problem with a new type of generative models that support both single-step and multi-step sampling. In the following, we extend the formulation of consistency models by Song et al. (2023) to accommodate conditioning information, such as data \mathbf{x} or a jointly learned embedding $h(\mathbf{x})$ (Radev et al., 2020).

3.1. Conditional Consistency Models

The consistency function $f:(\theta_t,t;\mathbf{x})\mapsto\theta_\varepsilon$ maps points across the solution trajectory $\{\theta_t\}_{t\in[T,\varepsilon]}$ to the trajectory's origin θ_ε given a fixed conditioning variable \mathbf{x} and the probability flow ODE in Eq. 4. To achieve this with established score-based diffusion model architectures, we can use a free-form neural network $F_{\phi}(\theta,t;\mathbf{x})$ which is parameterized through skip connections of the form

$$f_{\phi}(\boldsymbol{\theta}, t; \mathbf{x}) = c_{\text{skip}}(t)\boldsymbol{\theta} + c_{\text{out}}(t)F_{\phi}(\boldsymbol{\theta}, t; \mathbf{x}),$$
 (5)

where $c_{\rm skip}(t)$ and $c_{\rm out}(t)$ are differentiable and fulfill the boundary conditions $c_{\rm skip}(\varepsilon)=1$ and $c_{\rm out}(\varepsilon)=0$. Consistency models are originally motivated as a distillation technique for diffusion models. However, Song et al. (2023) show that training consistency models in isolation is possible, and we base our method on their direct approach.

Once the consistency model has been trained, generating draws from the approximate posterior is straightforward by drawing samples from the noise distribution, $\theta_T \sim \mathcal{N}(\mathbf{0}, T^2\mathbf{I})$, which shall then be transformed into samples from the target distribution, like in a standard diffusion model. In contrast to diffusion models, however, we do not need to solve a sequence of differential equations for this transformation. Instead, we can use the learned consistency function f_{ϕ} to obtain the one-step target sample $\theta_{\varepsilon} = f_{\phi}(\theta_T, T; \mathbf{x})$. What is more, inference with consistency model is not actually limited to one-step sampling. In

fact, multi-step generation is possible with an iterative sampling procedure, which we will describe in the following. For a sequence of time points $\varepsilon = t_1 < t_2 < \cdots < t_K = T$ and initial noise $\theta_K \sim \mathcal{N}(\mathbf{0}, T^2\mathbf{I})$, we calculate

$$\boldsymbol{\theta}_k \leftarrow f_{\boldsymbol{\phi}}(\boldsymbol{\theta}_{k+1}, t_{k+1}; \mathbf{x}) + \sqrt{t_k^2 - \varepsilon^2} \mathbf{z}_k$$
 (6)

for k = K - 1, K - 2, ..., 1, where $\mathbf{z}_k \sim \mathcal{N}(\mathbf{0}, \mathbf{I})$ and K - 1 is the number of sampling steps (Song & Dhariwal, 2023; Song et al., 2023). The resulting sample is usually better than a one-step sample: Adjusting the number of steps trades compute against sample quality (Song et al., 2023).

3.2. Consistency Models for SBI

Originally developed for image generation, consistency models can be applied to learn arbitrary distributions. The free-form architecture enables the integration of specialized architectures for both the data x and the parameters θ . Due to the low number of passes required for sampling (in contrast to flow matching and diffusion models), more complex networks can be used while maintaining low inference time. In theory, consistency models combine the best of both worlds (see Table 1): Unconstrained networks for optimal adaptation to parameter structure and data modalities, while enabling fast inference speed with few network passes. This comes at the cost of explicit invertibility, which leads to hardships for computing the posterior density, as detailed in Section 3.4. In accordance with the taxonomy from Cranmer et al. (2020), we call our method consistency model posterior estimation (CMPE). While we focus on posterior estimation, using consistency models for likelihood emulation is a natural extension of our work.

As a consequence of its fundamentally different training objective, CMPE is not just a faster version of FMPE. Instead, it shows qualitative differences to FMPE beyond a much faster sampling speed: (i) In **Experiment 4**, we show that CMPE is less dependent on the neural network architecture than FMPE, making it a promising alternative when the optimal architecture for a task is not known; (ii) throughout our experiments, we observe good performance in the low-data regime, rendering CMPE an attractive method when training data is scarce. In fact, limited data availability is a common limiting factor for complex simulation programs in science (e.g., molecular dynamics; Kadupitiya et al., 2020) and engineering (Heringhaus et al., 2022).

3.3. Optimization Objective

We use the consistency training objective for CMPE,

we use the consistency training objective for CMT L,
$$\mathcal{L}_{\text{CMPE}}(\boldsymbol{\phi}, \boldsymbol{\phi}^{-}) = \mathbb{E}\left[\lambda(t_{i}) d(\mathbf{u}(\boldsymbol{\phi}, t_{i+1}; \mathbf{x}), \mathbf{u}(\boldsymbol{\phi}^{-}, t_{i}; \mathbf{x}))\right]$$
(7)

where $\lambda(t)$ is a weighting function, $d(\mathbf{u}, \mathbf{v})$ is a distance metric, $\mathbf{z} \sim \mathcal{N}(\mathbf{0}, \mathbf{I})$, and the arguments for the distance

metric amount to the outputs of the consistency function obtained at two neighboring time indices t_i and t_{i+1} ,

$$\mathbf{u}(\boldsymbol{\phi}, t_{i+1}; \mathbf{x}) = f_{\boldsymbol{\phi}}(\boldsymbol{\theta} + t_{i+1}\mathbf{z}, t_{i+1}; \mathbf{x})$$
(8)

$$\mathbf{u}(\boldsymbol{\phi}^-, t_i; \mathbf{x}) = f_{\boldsymbol{\phi}^-}(\boldsymbol{\theta} + t_i \mathbf{z}, t_i; \mathbf{x}). \tag{9}$$

The teacher's parameter vector ϕ^- is a copy of the student's parameter which is held constant during each step via a stopgrad operator, $\phi^- \leftarrow \text{stopgrad}(\phi)$. We follow Song & Dhariwal (2023) using $\lambda(t_i) = 1/(t_{i+1} - t_i)$ and $d(\mathbf{u}, \mathbf{v}) = \sqrt{\|\mathbf{u} - \mathbf{v}\|_2^2 + c^2} - c$ from the Pseudo-Huber metric family. Appendix A contains details on discretization and noise schedules.

3.4. Density Estimation

Using the change-of-variable formula, we can express the posterior density of a single-step sample as

$$p_{\varepsilon}(\boldsymbol{\theta} \mid \mathbf{x}) = p_{T}(\boldsymbol{\theta}_{T} = f_{\phi}^{-1}(\boldsymbol{\theta}_{\varepsilon}, T; \mathbf{x})) \left| \det \left(\frac{\partial \boldsymbol{\theta}_{T}}{\partial \boldsymbol{\theta}_{\varepsilon}} \right) \right|,$$
(10)

where $f_{\phi}^{-1}(\boldsymbol{\theta},T;\mathbf{x})$ is the *implicit* inverse of the consistency function and $\partial \boldsymbol{\theta}_T/\partial \boldsymbol{\theta}_{\varepsilon}$ is the resulting Jacobian. While we cannot explicitly evaluate $f_{\phi}^{-1}(\boldsymbol{\theta}_{\varepsilon},T;\mathbf{x})$, we can generate samples from $\boldsymbol{\theta}_T \sim \mathcal{N}(\mathbf{0},T^2\mathbf{I})$ and use autodiff for evaluating the Jacobian because the consistency surrogate f_{ϕ} is differentiable. Thus, we cannot directly evaluate the posterior density at *arbitrary* $\boldsymbol{\theta}$. Yet, evaluating the density at a set of S posterior draws $\{\boldsymbol{\theta}_{\varepsilon}\}_{s=1}^{S}$ suffices for crucial downstream tasks, such as marginal likelihood estimation (Radev et al., 2023a), neural importance sampling (Dax et al., 2023a), or self-consistency losses (Schmitt et al., 2023a).

For the purpose of *multi-step sampling*, the latent variables $\theta_K, \theta_{K-1}, \dots, \theta_1$ form a Markov chain with a change-of-variables (CoV) given by Köthe (2023):

$$p(\boldsymbol{\theta}_1 \mid \mathbf{x}) = p(\boldsymbol{\theta}_K) \prod_{k=2}^K \frac{p(\boldsymbol{\theta}_{k-1} \mid \boldsymbol{\theta}_k, \mathbf{x})}{p(\boldsymbol{\theta}_k \mid \boldsymbol{\theta}_{k-1}, \mathbf{x})}.$$
 (11)

Due to Eq. 6, the backward conditionals are given by $p(\theta_{k-1} | \theta_k, \mathbf{x}) = \mathcal{N}\left(f_\phi(\theta_k, t_k; \mathbf{x}), (t_k^2 - \varepsilon^2)\mathbf{I}\right)$. Unfortunately, the forward conditionals $p(\theta_k | \theta_{k-1}, \mathbf{x})$ are not available in closed form, but we could learn an amortized surrogate model $q(\theta_k | \theta_{k-1})$ capable of single-shot density estimation based on a data set of execution paths $\{\theta_{1:K}\}$. This method would work well for relatively low-dimensional θ , which are common throughout scientific applications, but may diminish the efficiency gains of CMPE in higher dimensions. We leave an extensive evaluation of different surrogate density models to future work.

3.5. Choosing the Number of Sampling Steps

The design of consistency models enables one-step sampling (see Eq. 6). In practice, however, using two steps

significantly increases the sample quality in image generation tasks (Song & Dhariwal, 2023). We observe that few-step sampling with approximately K=5-10 steps provides the best trade-off between sample quality and compute, particularly in low-dimensional problems. This is roughly comparable to the speed of one-step estimators like affine coupling flows or neural spline flows in **Experiments 1–3** (see Figure 3). The number of steps can be chosen at inference time, so practitioners can easily adjust this trade-off for a given situation. We noticed that approaching the maximum number of discretization steps used in training can lead to overconfident posterior distributions. This effect becomes even more pronounced when the maximum number of discretization steps during training is surpassed, which we therefore discourage based on our empirical results.

4. Empirical Evaluation

Our experiments cover three fundamental aspects of SBI. First, we perform an extensive evaluation on three lowdimensional experiments with bimodal posterior distributions from benchmarking suites for inverse problems (Lueckmann et al., 2021; Kruse et al., 2021). The simulationbased training phase is based on a fixed training set $\{(\mathbf{x}^{(m)}, \pmb{\theta}_*^{(m)})\}_{m=1}^M$ of M tuples of data sets $\mathbf{x}^{(m)}$ and corresponding data-generating parameters (aka. ground-truths) $\theta_{\star}^{(m)}$. Second, we focus on an image denoising example which serves as a sufficiently high-dimensional case study in the context of SBI (Ramesh et al., 2022; Pacchiardi & Dutta, 2022). Third, we apply our CMPE method to a computationally challenging scientific model of tumor spheroid growth and showcase its superior performance for a non-trivial scientific simulator (Jagiella et al., 2017). We implement all experiments using the BayesFlow Python library for amortized Bayesian workflows (Radev et al., 2023b).

Evaluation metrics. We evaluate the experiments based on well-established metrics to gauge the accuracy and calibration of the results. All metrics are computed on a test set of Junseen instances $\{(\mathbf{x}^{(j)}, \boldsymbol{\theta}_*^{(j)})\}_{i=1}^J$. In the following, S denotes the number of (approximate) posterior samples that we draw for each instance J. First, the easy-to-understand root mean squared error (RMSE) metric quantifies both the bias and variance of the approximate posterior samples across the test set as $\frac{1}{J}\sum_{j=1}^{J}\sqrt{\frac{1}{S}\sum_{s=1}^{S}\left(\boldsymbol{\theta}_{s}^{(j)}-\boldsymbol{\theta}_{*}^{(j)}\right)^{2}}$. Second, we estimate the squared maximum mean discrepancy (MMD; Gretton et al., 2012) between samples from the approximate vs. reference posterior, which is a kernel-based distance between distributions. Third, as a widely applied metric in SBI, the C2ST score uses an MLP classifier to distinguish samples from the approximate and reference posteriors. The resulting test accuracy of the classifier is the C2ST score, which ranges from 0.5 (worst; samples are indistinguishable) to 1 (best; samples are perfectly separable). Finally,

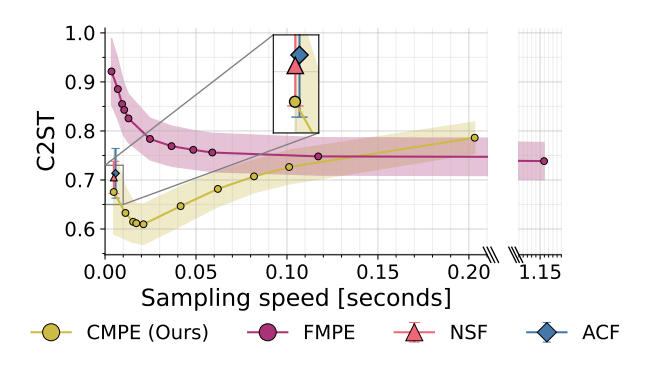


Figure 3: Experiment 1 (Gaussian Mixture Model). Average C2ST and its standard deviation over a test set of size J=100, as a function of each method's sampling speed for 1000 posterior draws. The sampling speed of FMPE and CMPE (Ours) is controlled by setting the number of inference steps K. CMPE (Ours) outperforms all other methods through both faster and better inference, as indexed by lower (better) C2ST scores. Mind the broken x-axis.

uncertainty calibration is assessed through simulation-based calibration (SBC; (Talts et al., 2018)): All uncertainty intervals $U_q(\boldsymbol{\theta} \mid \mathbf{x})$ of the true posterior $p(\boldsymbol{\theta} \mid \mathbf{x})$ are well calibrated for every quantile $q \in (0,1)$,

$$q = \iint \mathbf{I}[\boldsymbol{\theta}_* \in U_q(\boldsymbol{\theta} \mid \mathbf{x})] p(\mathbf{x} \mid \boldsymbol{\theta}_*) p(\boldsymbol{\theta}_*) d\boldsymbol{\theta}_* d\mathbf{x}, \quad (12)$$

where $I[\cdot]$ is the indicator function. Discrepancies from Eq. 12 indicate deficient calibration of an approximate posterior. The expected calibration error (ECE) aggregates the median SBC error of central credible intervals of 20 linearly spaced quantiles q, averaged across the test set.

Contender methods. We compare affine coupling flows (ACF; Dinh et al., 2016), neural spline flows (NSF; Durkan et al., 2019), flow matching posterior estimation (FMPE; Dax et al., 2023b), and consistency model posterior estimation (CMPE; ours). We use identical free-form neural networks for FMPE and CMPE to ensure comparability.

4.1. Experiment 1: Gaussian Mixture Model

We illustrate CMPE on a 2-dimensional Gaussian mixture model with two symmetrical components (Geffner et al., 2022; Schmitt et al., 2023a). The symmetrical components are equally weighted and have equal variance,

$$\theta \sim \mathcal{N}(\theta \mid \mathbf{0}, \mathbf{I}), \ \mathbf{x} \sim \frac{1}{2} \mathcal{N}(\mathbf{x} \mid \theta, \frac{\mathbf{I}}{2}) + \frac{1}{2} \mathcal{N}(\mathbf{x} \mid -\theta, \frac{\mathbf{I}}{2}),$$
(13)

where $\mathcal{N}(\cdot \mid \mu, \Sigma)$ is a Gaussian distribution with location μ and covariance matrix Σ . The resulting posterior distribution is bimodal and point-symmetric around the origin (see Figure 2 top-left). Each simulated data set \mathbf{x} consists of ten exchangeable observations $\{\mathbf{x}_1, \dots, \mathbf{x}_{10}\}$, and we train all

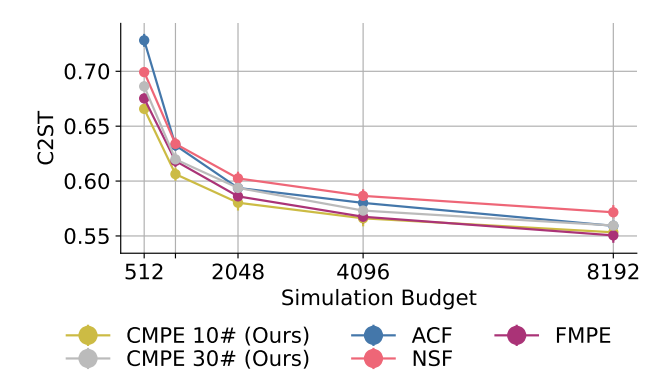


Figure 4: **Experiment 2 (Two Moons).** CMPE (Ours) with 10 sampling steps shows superior performance up to a training budget of 4096 instances. Plots show average C2ST and its standard error over a test set of size J=100.

architectures on M=1024 training simulations. We use a DeepSet (Zaheer et al., 2017) to learn 6 summary statistics for each data set jointly with the inference task.

Results. As displayed in Figure 2, both ACF and NSF fail to fit the bimodal posterior with separated modes. FMPE successfully forms disconnected posterior modes, but shows visible overconfidence through overly narrow posteriors. The visual sampling performance of CMPE is superior to all other methods. In this task, we observe that CMPE does not force us to choose between speed or performance relative to the other approximators. Instead, CMPE can outperform all other methods simultaneously with respect to both speed and performance, as evidenced by lower C2ST to the reference posterior across J=100 test instances (see Figure 3). If we tolerate slower sampling, CMPE achieves peak performance at K=10 inference steps. Most notably, CMPE outperforms 1000-step FMPE by a large margin, even though the latter is approximately $75 \times$ slower.

4.2. Experiment 2: Two Moons

This experiment studies the two moons benchmark (Greenberg et al., 2019; Lueckmann et al., 2021; Wiqvist et al., 2021; Radev et al., 2023a). The model is characterized by a bimodal posterior with two separated crescent moons for the observed point $\mathbf{x}_{\text{obs}} = (0,0)^{\top}$ which a posterior approximator needs to recover. We repeat the experiment for different training budgets $M \in \{512, 1024, 2048, 4096, 8192\}$ to assess the performance of each method under varying data availability. While M = 512 is a very small budget for the two moons benchmark, M = 8192 is considered sufficient.

Results. Trained on a simulation budget of M=1024 examples, CMPE consistently explores both crescent moons and successfully captures the local patterns of the posterior (see Figure 2, middle row). Both the affine coupling flow

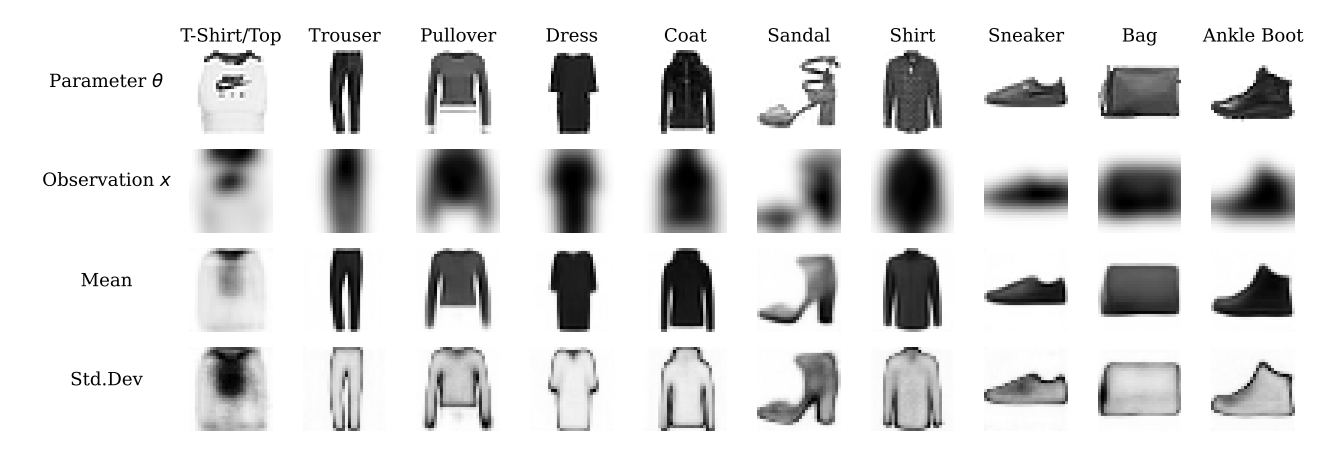


Figure 5: **Experiment 4**. CMPE denoising results from each class of Fashion MNIST obtained using a U-Net architecture and two-step sampling. A training set of 60 000 images was used. *First row:* Original image acting as the "parameters" of the noisy camera simulator. *Second row:* Blurred image, acting as the output of the camera simulator. *Third and fourth row:* Means and standard deviations of the posteriors estimated from the corresponding blurry "observations". *Note:* For standard deviations, darker regions indicate larger variability in the outputs. Adapted from Radev et al. (2023a).

and the neural spline flow fail to fully separate the modes. Most notably, if we aim to achieve fast sampling speed with FMPE by reducing the number of sampling steps during inference, FMPE shows visible overconfidence with 30 sampling steps and markedly deficient approximate posteriors with 10 sampling steps. In stark contrast, CMPE excels in the few-step regime. Figure 4 illustrates that all architectures benefit from a larger training budget. CMPE with 10 steps emerges as the superior architecture in the low- and medium- data regime up to M=4096 training instances. Many-step FMPE outperforms the other approximators for the largest training budget of M=8192 instances. Keep in mind, however, that many-step FMPE is approximately $30\text{--}70\times$ slower than ACF, NSF, and CMPE in this task.

4.3. Experiment 3: Inverse Kinematics

Proposed as a benchmarking task for inverse problems by Kruse et al. (2021), the inverse kinematics model aims to reconstruct the configuration $(\theta_1,\theta_2,\theta_3,\theta_4)=\pmb{\theta}\in\mathbb{R}^4$ of a multi-jointed 2D arm for a given end position $\mathbf{x}\in\mathbb{R}^2$ (see Figure 2, bottom left). The forward process $g:\pmb{\theta}\mapsto\mathbf{x}$ takes as inputs the initial height θ_1 of the arm's base, as well as the angles $\theta_2,\theta_3,\theta_4$ at its three joints. The inverse problem asks for the posterior distribution $p(\pmb{\theta}\mid\mathbf{x})$, which represents all arm configurations $\pmb{\theta}$ that end at the observed 2D position \mathbf{x} of the arm's end effector. The parameters follow a Gaussian prior $\pmb{\theta}\sim\mathcal{N}(\mathbf{0},\pmb{\sigma}^2\mathbf{I})$ with $\pmb{\sigma}^2=(\frac{1}{16},\frac{1}{4},\frac{1}{4},\frac{1}{4})$. While the parameter space in this task is 4-dimensional, we can readily plug any parameter estimate $\hat{\pmb{\theta}}$ into the forward simulator g to get the corresponding end effector position $g(\hat{\pmb{\theta}})=\hat{\mathbf{x}}\in\mathbb{R}^2$, which is easy to visualize and interpret.

Results. On the challenging small training budget of

M=1024 training examples, CMPE with K=30 sampling steps clearly outperforms all other methods while maintaining fast inference (see Figure 2).

4.4. Experiment 4: Bayesian Denoising

This experiment demonstrates the feasibility of CMPE for a high-dimensional inverse problem, namely, Bayesian denoising on the Fashion MNIST data set. The unknown parameter $\theta \in \mathbb{R}^{784}$ is the flattened original image, and the observation $\mathbf{x} \in \mathbb{R}^{784}$ is a blurred and flattened version of the crisp image from a simulated noisy camera (Ramesh et al., 2022; Pacchiardi & Dutta, 2022; Radev et al., 2023a).

We compare CMPE and FMPE in a standard and a small data regime. As both methods allow for free-form architectures, we can assess the effect of the architectural choices on the results. Therefore, we evaluate both methods using a suboptimal naïve architecture and the established U-Net (Ronneberger et al., 2015) architecture.

Neural architectures. The naïve architecture consists of a convolutional neural network (CNN; LeCun et al., 2015) to convert the observation into a vector of latent summary statistics. We concatenate input vector, summary statistics, and a time embedding and feed them into a multi-layer perceptron (MLP) with four hidden layers consisting of 2048 units each. This corresponds to a situation where the structure of the observation (i.e., image data) is known, but the structure of the parameters is unknown or does not inform a bespoke network architecture.

In this example, however, we can leverage the prior knowledge that our parameters are images. Specifically, we can incorporate inductive biases into our network architecture

Table 2: **Experiment 4**: RMSE and MMD between the ground-truth image vs. 100 draws from the approximators trained on 2 000 and 60 000 training images, aggregated over 100 test images. For MMD, we draw one denoised sample per test image and calculate the MMD between the denoised samples and the original images. *Time* per draw.

Models		SE ↓ 60 000	MMD (± SD) 2 000	$[\times 10^{-3}] \downarrow 60000$	Time ↓
FMPE (Ours)	0.836 0.388	0.597 0.293	171.53 ± 1.61 102.09 ± 3.24	95.26 ± 1.21 57.90 ± 1.59	15.4ms 0.3 ms
FMPE (Ours)	0.278 0.311	0.217 0.238	17.38 ± 0.10 18.49 ± 0.12	14.50 ± 0.05 16.08 ± 0.05	1

by choosing a U-Net architecture which is optimized for image processing (i.e., an adapted version of Nain, 2022). Again, a CNN learns a summary vector of the noisy observation, which is then concatenated with a time embedding into the condition vector for the neural density estimator.

Results. We report the aggregated RMSE, MMD, and the time per sample for both methods and architectures (Table 2). FMPE is not able to generate good samples for the naïve architecture, whereas CMPE produces acceptable samples even in this suboptimal setup. This reduced susceptibility to suboptimal architectures might become a valuable feature in high-dimensional problems where the structure of the parameters cannot be exploited. The U-Net architecture enables good sample quality for both methods, highlighting the advantages of free-form architectures. The MMD values align well with a visual assessment of the sample quality, therefore we deem it an informative metric to compare the results (see Section C.4 for visual inspection). The U-Net architecture paired with a large training set provides detailed and versatile samples of similar quality for CMPE and FMPE. In all cases, CMPE exhibits significantly lower inference time as only two network passes are required for sampling, while achieving better or competitive quality.

4.5. Experiment 5: Tumor Spheroid Growth

We conclude our empirical evaluation with a complex multiscale model of 2D tumor spheroid growth (Jagiella et al., 2017) with 7 unknown parameters (taken from pyABC, 2017). Crucially, running simulations from this model on standard hardware is rather expensive (≈ 1 minute for a single run on a consumer-grade computer), so there is a desire for methods that can provide reasonable estimates for a limited offline training budget. Here, we compare the performance of the four contender methods in this paper on a fixed training set of $M=19\,600$ simulations with J=400 simulations as a test set to compute performance metrics. Across all methods, we use a hybrid LSTM-Transformer architecture to transform high-dimensional expert data of variable length into fixed length summary vectors $h(\mathbf{x})$.

Table 3: **Experiment 5.** RMSE, ECE, and sampling time are computed for 2000 posterior samples, aggregated over 400 unseen test instances. Max ECE denotes the worst-case marginal calibration error across all 7 model parameters.

Model	RMSE ↓	Max ECE↓	Time ↓
ACF	0.589	0.021	1.07s
NSF	0.590	0.027	1.95s
FMPE 30#	0.582	0.222	17.13s
FMPE 1000#	0.583	0.057	500.90s
CMPE 2# (Ours)	0.616	0.064	2.16s
CMPE 30# (Ours)	0.577	0.018	18.33s

Appendix C.5 provides more details on the neural network architectures and training hyperparameters.

Results. CMPE outperforms the alternative neural methods via better accuracy and calibration, as indexed by lower RMSE and ECE on 400 unseen test instances (see Table 3). The speed of the simpler ACF is unmatched by the other methods. In direct comparison to its free-form contender FMPE, CMPE simultaneously exhibits (i) a slightly higher accuracy; (ii) a drastically improved calibration; and (iii) much faster sampling (see Figure 6 in the Appendix). For this model, FMPE did not achieve satisfactory calibration performance with up to K=100 inference steps, so Table 3 reports the best FMPE results for K=1000 steps.

5. Conclusion

We presented consistency model posterior estimation (CMPE), a state-of-the-art approach to perform accurate simulation-based Bayesian inference on large-scale models while achieving fast inference speed. CMPE enhances the capabilities of neural posterior estimation by combining the free-form neural architecture property of diffusion models and flow matching with high-performing few-step sampling. To assess the effectiveness of CMPE, we applied it to a set of 3 low-dimensional benchmark tasks that allow intuitive visual inspection, as well as a high-dimensional Bayesian denoising experiment and a scientific tumor growth model. Across all experiments, CMPE consistently outperforms all other methods based on a holistic assessment of posterior accuracy, calibration, and inference speed.

Future work might aim to further reduce the number of sampling steps towards one-step inference, for instance, via extensive automated hyperparameter optimization or tailored training schemes for CMPE. Overall, our results prove the potential of CMPE as a novel simulation-based inference tool, rendering it a new contender for simulation-based inference workflows in science and engineering.

Acknowledgments

We thank Lasse Elsemüller for insightful feedback and thought-provoking ideas. MS acknowledges the funding of the Cyber Valley Research Fund (grant number: CyVy-RF-2021-16) and the Deutsche Forschungsgemeinschaft (DFG, German Research Foundation) under Germany's Excellence Strategy EXC-2075 - 390740016 (the Stuttgart Cluster of Excellence SimTech). MS additionally thanks the Google Cloud Research Credits program and the European Laboratory for Learning and Intelligent Systems (EL-LIS) PhD program for support. VP acknowledges funding by the German Academic Exchange Service (DAAD) and the German Federal Ministry of Education and Research (BMBF) through the funding programme "Konrad Zuse Schools of Excellence in Artificial Intelligence" (ELIZA) and support by the state of Baden-Württemberg through bwHPC. VP acknowledges support by the Bundesministerium fuer Wirtschaft und Klimaschutz (BMWK, German Federal Ministry for Economic Affairs and Climate Action) as part of the German government's 7th energy research program "Innovations for the energy transition" under the 03ETE039I HiBRAIN project (Holistic method of a combined data- and model-based Electrode design supported by artificial intelligence).

Impact statement

This paper presents work whose goal is to advance the field of machine learning. There are many potential societal consequences of our work, none of which we feel must be specifically highlighted here.

References

- Ardizzone, L., Kruse, J., Wirkert, S., Rahner, D., Pellegrini, E. W., Klessen, R. S., Maier-Hein, L., Rother, C., and Köthe, U. Analyzing inverse problems with invertible neural networks. In *Intl. Conf. on Learning Representations*, 2019.
- Avecilla, G., Chuong, J. N., Li, F., Sherlock, G., Gresham, D., and Ram, Y. Neural networks enable efficient and accurate simulation-based inference of evolutionary parameters from adaptation dynamics. *PLoS Biology*, 20 (5):e3001633, 2022.
- Batzolis, G., Stanczuk, J., Schönlieb, C.-B., and Etmann, C. Conditional image generation with score-based diffusion models, 2021.
- Bieringer, S., Butter, A., Heimel, T., Höche, S., Köthe, U., Plehn, T., and Radev, S. T. Measuring qcd splittings with invertible networks. *SciPost Physics*, 10(6):126, 2021.
- Butter, A., Plehn, T., Schumann, S., Badger, S., Caron, S.,

- Cranmer, K., Di Bello, F. A., Dreyer, E., Forte, S., Ganguly, S., et al. Machine learning and lhc event generation. *arXiv preprint arXiv:2203.07460*, 2022.
- Cranmer, K., Brehmer, J., and Louppe, G. The frontier of simulation-based inference. *Proceedings of the National Academy of Sciences*, 2020.
- Dax, M., Green, S. R., Gair, J., Pürrer, M., Wildberger, J., Macke, J. H., Buonanno, A., and Schölkopf, B. Neural importance sampling for rapid and reliable gravitational-wave inference. *Physical Review Letters*, 130(17), April 2023a. ISSN 1079-7114. doi: 10.1103/physrevlett.130. 171403. URL http://dx.doi.org/10.1103/PhysRevLett.130.171403.
- Dax, M., Wildberger, J., Buchholz, S., Green, S. R., Macke, J. H., and Schölkopf, B. Flow matching for scalable simulation-based inference, 2023b.
- Deistler, M., Goncalves, P. J., and Macke, J. H. Truncated proposals for scalable and hassle-free simulation-based inference. *arXiv* preprint, 2022.
- Dinh, L., Sohl-Dickstein, J., and Bengio, S. Density estimation using real nvp. *arXiv preprint arXiv:1605.08803*, 2016.
- Durkan, C., Bekasov, A., Murray, I., and Papamakarios, G. Neural spline flows. Advances in neural information processing systems, 32, 2019.
- Durkan, C., Murray, I., and Papamakarios, G. On contrastive learning for likelihood-free inference. In *International Conference on Machine Learning*. PMLR, 2020.
- Elsemüller, L., Olischläger, H., Schmitt, M., Bürkner, P.-C., Köthe, U., and Radev, S. T. Sensitivity-aware amortized Bayesian inference, 2023a. arXiv:2310.11122.
- Elsemüller, L., Schnuerch, M., Bürkner, P.-C., and Radev, S. T. A deep learning method for comparing bayesian hierarchical models, 2023b.
- Engel, J., Resnick, C., Roberts, A., Dieleman, S., Norouzi, M., Eck, D., and Simonyan, K. Ddsp: Differentiable digital signal processing. In *International Conference on Learning Representations*, 2020.
- Geffner, T., Papamakarios, G., and Mnih, A. Compositional score modeling for simulation-based inference, 2022.
- Ghaderi-Kangavari, A., Rad, J. A., and Nunez, M. D. A general integrative neurocognitive modeling framework to jointly describe EEG and decision-making on single trials. *Computational Brain and Behavior*, 2023. doi: 10.1007/s42113-023-00167-4.

- Gonçalves, P. J., Lueckmann, J.-M., Deistler, M., et al. Training deep neural density estimators to identify mechanistic models of neural dynamics. *Elife*, 2020.
- Goodfellow, I., Pouget-Abadie, J., Mirza, M., Xu, B., Warde-Farley, D., Ozair, S., Courville, A., and Bengio, Y. Generative adversarial nets. In Ghahramani, Z., Welling, M., Cortes, C., Lawrence, N., and Weinberger, K. (eds.), Advances in Neural Information Processing Systems, volume 27. Curran Associates, Inc., 2014.
- Greenberg, D., Nonnenmacher, M., and Macke, J. Automatic posterior transformation for likelihood-free inference. In *International Conference on Machine Learning*, 2019.
- Gretton, A., Borgwardt, K., Rasch, M., Schölkopf, B., and Smola, A. A Kernel Two-Sample Test. *The Journal of Machine Learning Research*, 13:723–773, 2012.
- Heringhaus, M. E., Zhang, Y., Zimmermann, A., and Mikelsons, L. Towards reliable parameter extraction in mems final module testing using bayesian inference. *Sensors*, 22(14):5408, July 2022. ISSN 1424-8220. doi: 10.3390/s22145408. URL http://dx.doi.org/10.3390/s22145408.
- Ho, J., Jain, A., and Abbeel, P. Denoising diffusion probabilistic models. In *Advances in Neural Information Processing Systems*, volume 33, pp. 6840–6851, 2020.
- Jagiella, N., Rickert, D., Theis, F. J., and Hasenauer, J. Parallelization and high-performance computing enables automated statistical inference of multi-scale models. *Cell* systems, 4(2):194–206, 2017.
- Kadupitiya, J., Sun, F., Fox, G., and Jadhao, V. Machine learning surrogates for molecular dynamics simulations of soft materials. *Journal of Computational Science*, 42: 101107, 2020. doi: 10.1016/j.jocs.2020.101107.
- Karras, T., Aittala, M., Aila, T., and Laine, S. Elucidating the design space of diffusion-based generative models. *Advances in Neural Information Processing Systems*, 35: 26565–26577, 2022.
- Köthe, U. A review of change of variable formulas for generative modeling. *arXiv preprint arXiv:2308.02652*, 2023.
- Kruse, J., Ardizzone, L., Rother, C., and Köthe, U. Benchmarking invertible architectures on inverse problems. 2021. Workshop on Invertible Neural Networks and Normalizing Flows (ICML 2019).
- Lavin, A., Zenil, H., Paige, B., et al. Simulation intelligence: Towards a new generation of scientific methods. *arXiv* preprint, 2021.

- LeCun, Y., Bengio, Y., and Hinton, G. Deep learning. *Nature*, 521(7553):436–444, 2015. ISSN 1476-4687. doi: 10.1038/nature14539. URL http://dx.doi.org/10.1038/nature14539.
- Lipman, Y., Chen, R. T. Q., Ben-Hamu, H., Nickel, M., and Le, M. Flow matching for generative modeling. In *The 11th International Conference on Learning Representations*, 2023. URL https://openreview.net/forum?id=PqvMRDCJT9t.
- Liu, X., Gong, C., and Liu, Q. Flow straight and fast: Learning to generate and transfer data with rectified flow, 2022.
- Lueckmann, J.-M., Gonçalves, P. J., Bassetto, G., Öcal, K., Nonnenmacher, M., and Macke, J. H. Flexible statistical inference for mechanistic models of neural dynamics. In *31st NeurIPS Conference Proceedings*, 2017.
- Lueckmann, J.-M., Boelts, J., Greenberg, D. S., Gonçalves, P. J., and Macke, J. H. Benchmarking simulation-based inference. arXiv preprint, 2021.
- Nain, A. K. Keras documentation: Denoising diffusion probabilistic model. https://keras.io/examples/generative/ddpm/, 2022. Accessed: 2023-11-27.
- Pacchiardi, L. and Dutta, R. Score matched neural exponential families for likelihood-free inference. *J. Mach. Learn. Res.*, 23:38–1, 2022.
- Papamakarios, G. and Murray, I. Fast ε -free inference of simulation models with bayesian conditional density estimation. *Advances in neural information processing systems*, 29, 2016.
- Papamakarios, G., Nalisnick, E., Rezende, D. J., Mohamed, S., and Lakshminarayanan, B. Normalizing flows for probabilistic modeling and inference. *J. Mach. Learn. Res.*, 22(1), jan 2021. ISSN 1532-4435.
- pyABC. pyABC documentation, multiscale model: Tumor spheroid growth. https://pyabc.readthedocs.io/en/latest/examples/multiscale_agent_based.html, 2017. Accessed: 2023-12-07.
- Radev, S. T., Mertens, U. K., Voss, A., Ardizzone, L., and Köthe, U. Bayesflow: Learning complex stochastic models with invertible neural networks. *IEEE transactions on* neural networks and learning systems, 2020.
- Radev, S. T., D'Alessandro, M., Mertens, U. K., Voss, A., Köthe, U., and Bürkner, P.-C. Amortized bayesian model comparison with evidential deep learning. *IEEE Transac*tions on Neural Networks and Learning Systems, 2021a.

- Radev, S. T., Graw, F., Chen, S., Mutters, N. T., Eichel, V. M., Bärnighausen, T., and Köthe, U. Outbreakflow: Model-based bayesian inference of disease outbreak dynamics with invertible neural networks and its application to the covid-19 pandemics in germany. *PLoS computational biology*, 2021b.
- Radev, S. T., Schmitt, M., Pratz, V., Picchini, U., Köthe, U., and Bürkner, P.-C. JANA: Jointly Amortized Neural Approximation of Complex Bayesian Models. In Evans, R. J. and Shpitser, I. (eds.), Proceedings of the 39th Conference on Uncertainty in Artificial Intelligence, volume 216 of Proceedings of Machine Learning Research, pp. 1695–1706. PMLR, 2023a.
- Radev, S. T., Schmitt, M., Schumacher, L., Elsemüller, L., Pratz, V., Schälte, Y., Köthe, U., and Bürkner, P.-C. Bayesflow: Amortized bayesian workflows with neural networks. *Journal of Open Source Software*, 8 (89):5702, 2023b. doi: 10.21105/joss.05702. URL https://doi.org/10.21105/joss.05702.
- Ramesh, P., Lueckmann, J.-M., Boelts, J., Tejero-Cantero, Á., Greenberg, D. S., Gonçalves, P. J., and Macke, J. H. Gatsbi: Generative adversarial training for simulationbased inference. arXiv preprint arXiv:2203.06481, 2022.
- Rezende, D. J. and Mohamed, S. Variational inference with normalizing flows. In *Proceedings of the 32nd International Conference on International Conference on Machine Learning Volume 37*, ICML'15, pp. 1530–1538. JMLR.org, 2015.
- Rombach, R., Blattmann, A., Lorenz, D., Esser, P., and Ommer, B. High-resolution image synthesis with latent diffusion models. In *Proceedings of the IEEE/CVF Conference on Computer Vision and Pattern Recognition (CVPR)*, pp. 10684–10695, 2022.
- Ronneberger, O., Fischer, P., and Brox, T. U-net: Convolutional networks for biomedical image segmentation. In Navab, N., Hornegger, J., Wells, W. M., and Frangi, A. F. (eds.), *Medical Image Computing and Computer-Assisted Intervention MICCAI 2015*, pp. 234–241, Cham, 2015. Springer International Publishing. ISBN 978-3-319-24574-4.
- Schmitt, M., Habermann, D., Bürkner, P.-C., Koethe, U., and Radev, S. T. Leveraging self-consistency for data-efficient amortized Bayesian inference. In *NeurIPS UniReps: the First Workshop on Unifying Representations in Neural Models*, 2023a.
- Schmitt, M., Radev, S. T., and Bürkner, P.-C. Fuse it or lose it: Deep fusion for multimodal simulation-based inference, 2023b. arXiv:2311.10671.

- Sharrock, L., Simons, J., Liu, S., and Beaumont, M. Sequential neural score estimation: Likelihood-free inference with conditional score based diffusion models, 2022.
- Shiono, T. Estimation of agent-based models using Bayesian deep learning approach of BayesFlow. *Journal of Economic Dynamics and Control*, 125:104082, 2021.
- Song, Y. and Dhariwal, P. Improved Techniques for Training Consistency Models, October 2023.
- Song, Y. and Ermon, S. Generative modeling by estimating gradients of the data distribution. In *Proceedings of the 33rd International Conference on Neural Information Processing Systems*, 2019.
- Song, Y., Sohl-Dickstein, J., Kingma, D. P., Kumar, A., Ermon, S., and Poole, B. Score-based generative modeling through stochastic differential equations. In *International Conference on Learning Representations*, 2021.
- Song, Y., Dhariwal, P., Chen, M., and Sutskever, I. Consistency models. In *International Conference on Machine Learning*, 2023.
- Talts, S., Betancourt, M., Simpson, D., Vehtari, A., and Gelman, A. Validating bayesian inference algorithms with simulation-based calibration. *arXiv* preprint, 2018.
- von Krause, M., Radev, S. T., and Voss, A. Mental speed is high until age 60 as revealed by analysis of over a million participants. *Nature Human Behaviour*, 6(5):700–708, May 2022. doi: 10.1038/s41562-021-01282-7.
- Vondrick, C., Pirsiavash, H., and Torralba, A. Generating videos with scene dynamics. *Advances in Neural Information Processing Systems*, 29, 2016.
- Wiqvist, S., Frellsen, J., and Picchini, U. Sequential neural posterior and likelihood approximation. *arXiv preprint*, 2021.
- Zaheer, M., Kottur, S., Ravanbakhsh, S., Poczos, B., Salakhutdinov, R., and Smola, A. Deep sets, 2017.

A. Consistency training details

Table 4 details all functions and parameters required for training. Except for the choice of parameters s_0 , s_1 , ε , T_{max} and σ_{data} we exactly follow the design choices proposed by Song & Dhariwal (2023), which improved our results compared to the choices in Song et al. (2023). Song & Dhariwal (2023) showed that that the Exponential Moving Average of the teacher's parameter ϕ^- should not be used in Consistency Training, therefore we omitted it in this paper.

Table 4: **Design choices**: Table and values adapted to our notation from Song & Dhariwal (2023, Table 1).

Metric in consistency loss	$d(\mathbf{x}, \mathbf{y}) = \sqrt{\ \mathbf{x} - \mathbf{y}\ _2^2 + c^2 - c}$
Discretization curriculum	$N(k) = \min(s_0 2^{\lfloor k/K' \rfloor}, s_1) + 1 \text{ where } K' = \lfloor K/(\log_2 \lfloor s_1/s_0 \rfloor + 1) \rfloor$
Noise schedule	t_i , where $i \sim p(i)$ and $p(i) \sim \operatorname{erf}\left(\frac{\log(t_{i+1}) - P_{\operatorname{mean}}}{\sqrt{2}P_{\operatorname{std}}}\right) - \operatorname{erf}\left(\frac{\log(t_i) - P_{\operatorname{mean}}}{\sqrt{2}P_{\operatorname{std}}}\right)$
Weighting function	$\lambda(t_i) = 1/(t_{i+1} - t_i)$
Skip connections	$c_{\rm skip}(t) = \sigma_{\rm data}^2/((t-\varepsilon)^2 + \sigma_{\rm data}^2), c_{\rm out}(t) = \sigma_{\rm data}(t-\varepsilon)/\sqrt{\sigma_{\rm data}^2 + t^2}$
	$s_0 = 10, s_1 = 50$ except where indicated otherwise
	$c = 0.00054\sqrt{d}$, where d is the dimensionality of θ
Parameters	$P_{\text{mean}} = -1.1, P_{\text{std}} = 2.0$
	$k \in {0, \dots, K-1}$, where K is the total training iterations
	$t_i = \left(\varepsilon^{1/\rho} + \frac{i+1}{N(k)-1} \left(T_{\text{max}}^{1/\rho} - \varepsilon^{1/\rho}\right)\right)^{\rho}, \rho = 7, \varepsilon = 0.001, T_{\text{max}} = 200$

B. Evaluation metrics

Especially for multi-modal distributions, some of the standard metrics may behave in unexpected ways. This impedes an interpretation of the results and can lead to misleading conclusions. In this section, we want to highlight the peculiarities of some of the metrics, and highlight where caution is necessary when they are applied to the presented benchmarks.

B.1. C2ST

Being an expressive classifier, C2ST is most sensitive to regions where there is no overlap between distributions. In our experiments, this results in a pronounced punishment of overconfident posteriors. For limited training data and distributions without sharp edges (e.g., the Gaussian mixture model), some overconfidence is usually given, as samples from the outer tails are simply not present in the training set. As the accuracy is used as a measure, a smaller number of very improbable samples (e.g., samples in the region between two modes) do not influence the results a lot.

In consequence, C2ST may deviate from the visual judgement in important ways. First, overconfident posteriors look more "precise", but are punished by C2ST. Second, samples between modes are very salient, but may not influence the results of C2ST a lot.

For distributions with sharp edges and more or less uniform density in a given mode, c2st is very capable in judging the overlap of two distributions, which then is a good measure of quality. This applies to the two-moons example, where we can observe the expected behavior of a larger training budget leading to more accurate results (Figure 4).

B.2. MMD

By capturing and comparing the moments of two distributions, MMD provides a more holistic view than C2ST. It is also applicable to a wider range of cases, as it generalizes to high dimensions. The exact behaviour can be controlled by choosing the kernel function. In our experiments, we observe MMD to be less sensitive for distributions with sharp edges (i.e., two moons), where C2ST seems to provide more reasonable results. We also observe a low sensitivity to samples between modes, leading to unexpected results compared to visual inspection.

B.3. Summary

Calculating meaningful metrics given only samples from two distributions is a challenging task. Ideally, the metrics would reward similar density and punish samples in the low-density regions of the reference distribution. Especially the latter seems to be hard to achieve. Even when metrics work fine for small deviations from the ideal distribution, the behaviour

for different forms of larger deviations, as they occur in challenging problems or cases with low training budget, might not be easily grasped or interpreted. That makes it difficult to compare different methods producing qualitatively different deviations (e.g., overconfidence vs. underconfidence) from the reference distribution.

C. Additional details and results

C.1. Experiment 1

Neural network details. All architectures use a summary network to learn fixed-length representations of the i.i.d. data $\mathbf{x} = \{\mathbf{x}_1, \dots, \mathbf{x}_{10}\}$. We implement this via a DeepSet (Zaheer et al., 2017) with 6-dimensional output. Both ACF and NSF use 4 coupling layers and train for 200 epochs with a batch size 32. CMPE relies on an MLP with 2 hidden layers of 256 units each, L2 regularization with weight 10^{-4} , 10% dropout and an initial learning rate of 10^{-4} . The consistency model is instantiated with the hyperparameters $s_0 = 10$, $s_1 = 1280$, $T_{\text{max}} = 1$. Training is based on 2000 epochs with batch size 64. FMPE and CMPE use an identical MLP, and the only difference is the initial learning rate of 10^{-5} for FMPE to alleviate instable training dynamics.

C.2. Experiment 2

Neural network details. CMPE uses an MLP with 2 layers of 256 units each, L2 regularization with weight 10^{-5} , 5% dropout, and an initial learning rate of $5 \cdot 10^{-4}$. The consistency model uses $s_0 = 10$, $s_1 = 50$, $T_{\text{max}} = 10$, and it is trained with a batch size of 64 for 5000 epochs. Both ACF and NSF use 6 coupling layers of 128 units each, kernel regularization with weight $\gamma = 10^{-4}$, and train for 200 epochs with a batch size 32. FMPE uses the same settings and training configuration as CMPE.

C.3. Experiment 3

Neural network details. CMPE relies on an MLP with 2 layers of 256 units each, L2 regularization with weight 10^{-5} , 5% dropout, and an initial learning rate of 5×10^{-4} . The consistency model uses $s_0 = 10$, $s_1 = 50$, and trains for 2000 epochs with a batch size of 32. FMPE uses the same MLP and training configuration as CMPE. Both ACF and NSF use 6 coupling layers of 128 units each, kernel regularization with weight $\gamma = 10^{-4}$, and train for 200 epochs with a batch size 32.

C.4. Experiment 4

We compare samples from a $2 \times 2 \times 2$ design: Two methods, CMPE and FMPE, are trained on two network architectures, a naïve architecture and a U-Net architecture, using 2 000 and 60 000 training images. Except for the batch size, which is 32 for 2 000 training images and 256 for 60 000 training images, all hyperparameters are held constant between all runs. We use an AdamW optimizer with a learning rate of $5 \cdot 10^{-4}$ and cosine decay for 20 000 iterations, rounded up to the next full epoch. As both methods use the same network sizes, this results in an approximately equal training time between methods (approximately 1-2 hours on a Tesla V100 GPU), with a significantly lower training time for the naïve architecture. **Neural network details.** For CMPE, we use $s_0 = 10$, $s_1 = 50$, $\sigma_{\text{data}}^2 = 0.25$ and two-step sampling. For FMPE, we follow Dax et al. (2023b) and use 248 network passes. Note that this is directly correlated with inference time: Choosing a lower value will make FMPE sampling faster, a larger value will slow down FMPE sampling.

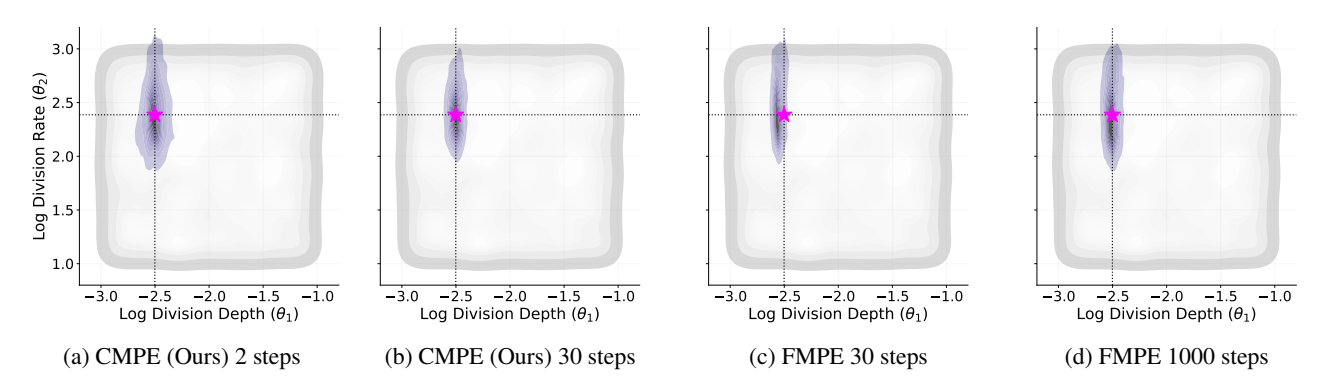


Figure 6: **Experiment 5.** Posterior draws for two parameters of the tumor growth model. Cross-hair and pink star indicate the ground-truth parameter that we aim to recover for one fixed data set x. The gray region depicts the prior distribution. CMPE (Ours) shows no visible bias even for two-step inference, but an improved sharpness when we increase the number of sampling steps to 30. In contrast, FMPE with 30 sampling steps (comparable speed to CMPE) yields a biased posterior. The posterior of FMPE with 1000 inference steps visibly improves but is orders of magnitude slower than CMPE with 30 steps.

C.5. Experiment 5

Neural network details. Both CMPE and FMPE use an MLP with 4 hidden layers of 512 units each and 20% dropout. CMPE and FMPE train for 1000 epochs with a batch size of 64. The consistency model uses $s_0 = 10, s_1 = 50, T_{\text{max}} = 50$. ACF and NSF employ a coupling architecture with learnable permutations, 6 coupling layers of 128 units each, 20% dropout, and 300 epochs of training with a batch size of 64.

The input data consists of multiple time series of different lengths. As proposed by Schmitt et al. (2023b) for SBI with heterogeneous data sources, we employ a *late fusion* scheme where the input modalities are first processed by individual embedding networks, and then fused. First, the data on tumor size growth curves enters an LSTM which produces a 16-dimensional representation of this modality. Second, the information about radial features is processed by a temporal fusion transformer with 4 attention heads, 64-dimensional keys, 128 units per fully-connected layer, and 10^{-4} L2 regularization on both weights and biases. These latent representations are then concatenated and further fed through a fully-connected two-layer perceptron of 256 units each, 10^{-4} L2 regularization on weights and biases, and 32 output dimensions.

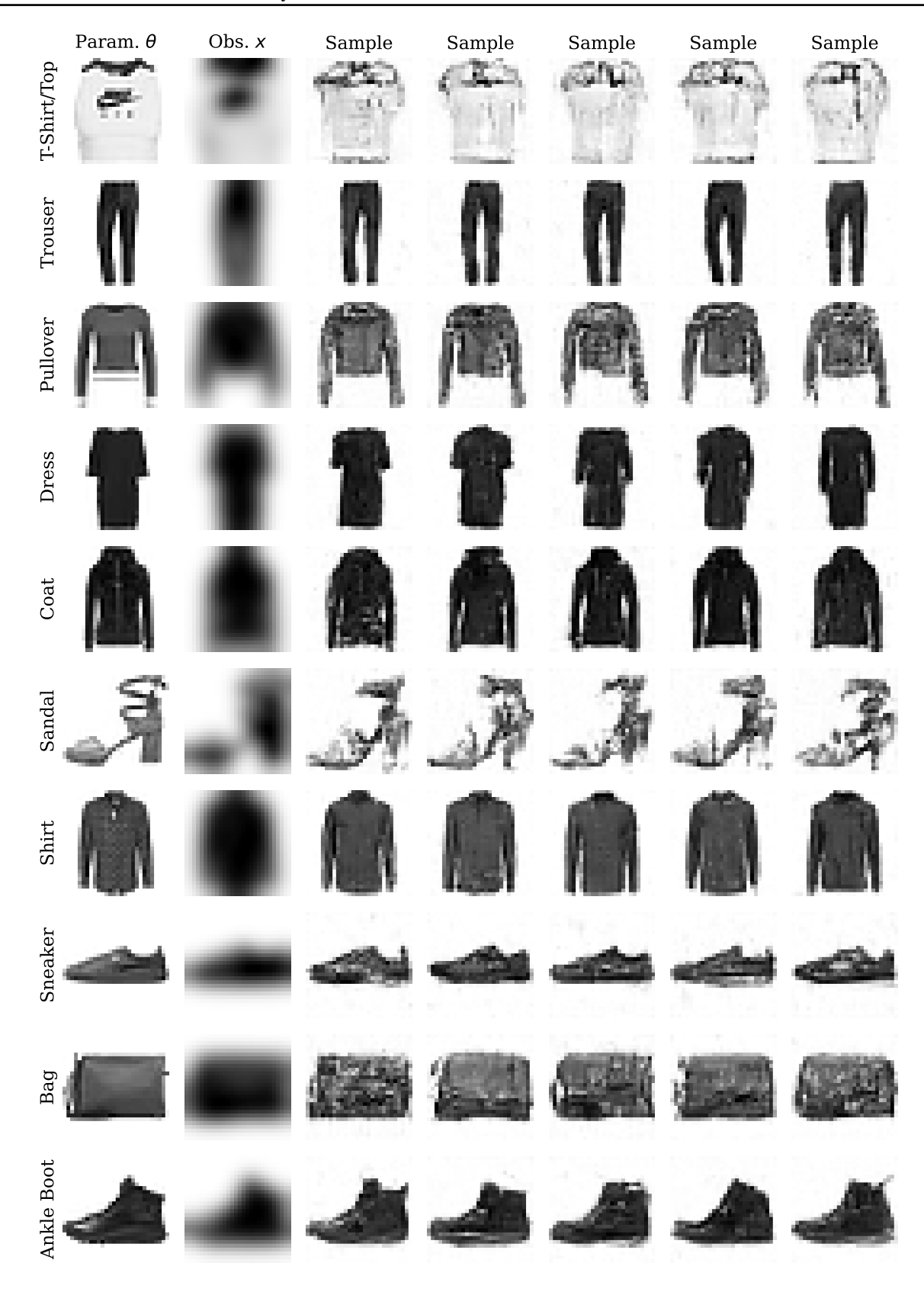


Figure 7: **CMPE - U-Net architecture - 2000 training images**. CMPE denoising results from each class of Fashion MNIST obtained using a U-Net architecture and two-step sampling. A small training set of 2000 images was used.

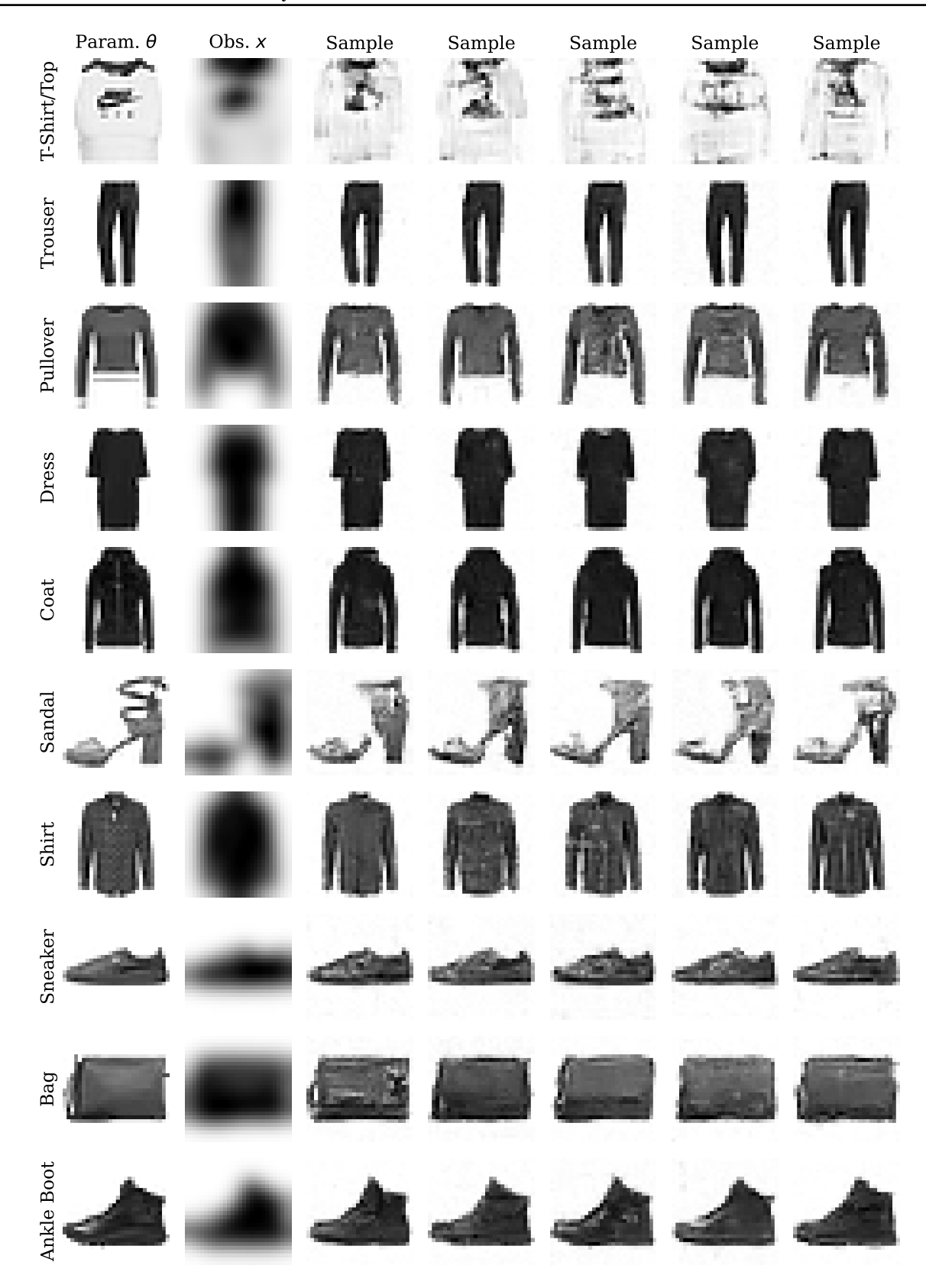


Figure 8: **CMPE - U-Net architecture - 60 000 training images**. CMPE denoising results from each class of Fashion MNIST obtained using a U-Net architecture and two-step sampling. A large training set of 60 000 images was used.

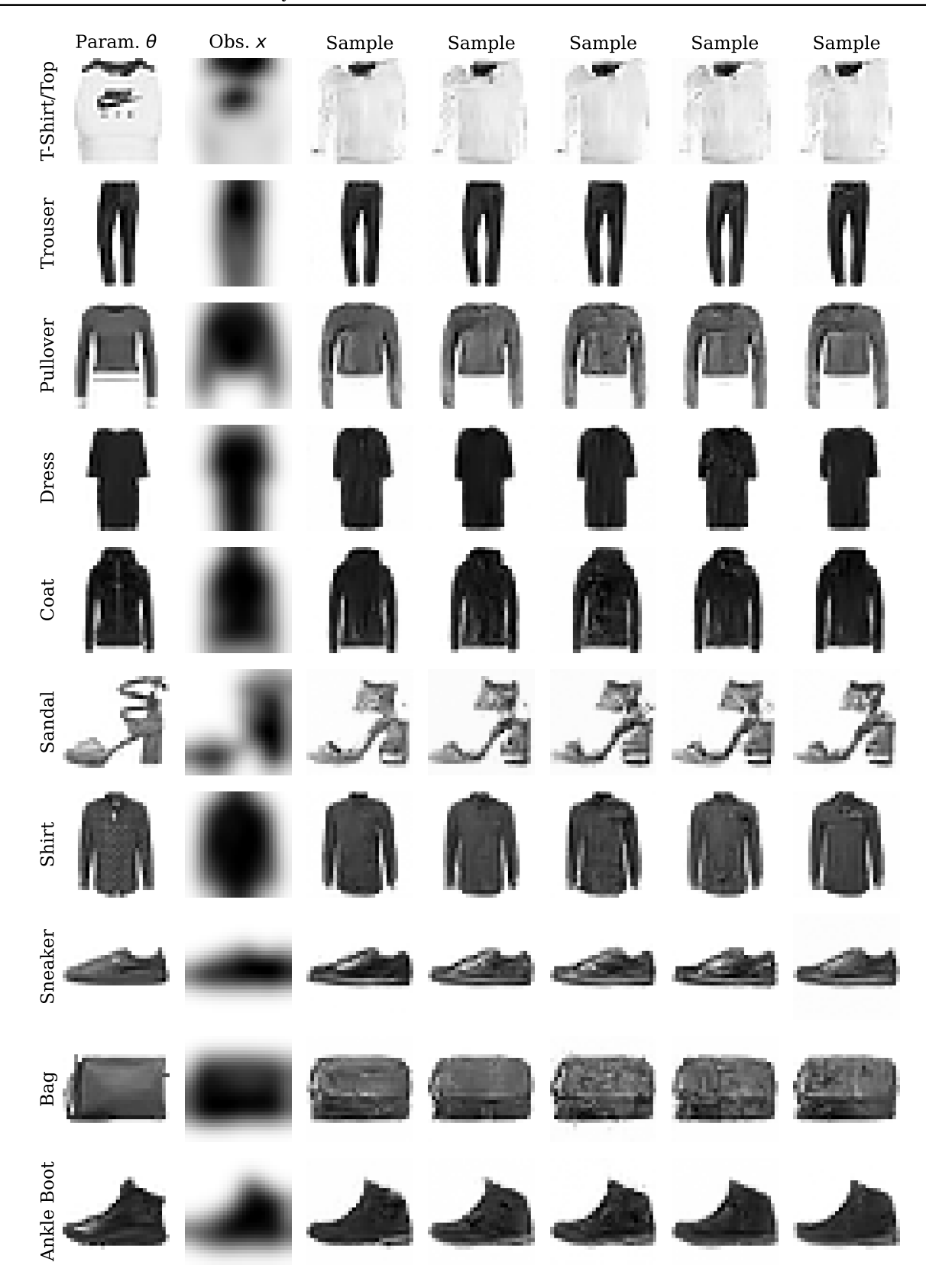


Figure 9: **FMPE - U-Net architecture - 2000 training images**. FMPE denoising results from each class of Fashion MNIST obtained using a U-Net architecture. A small training set of 2000 images was used.

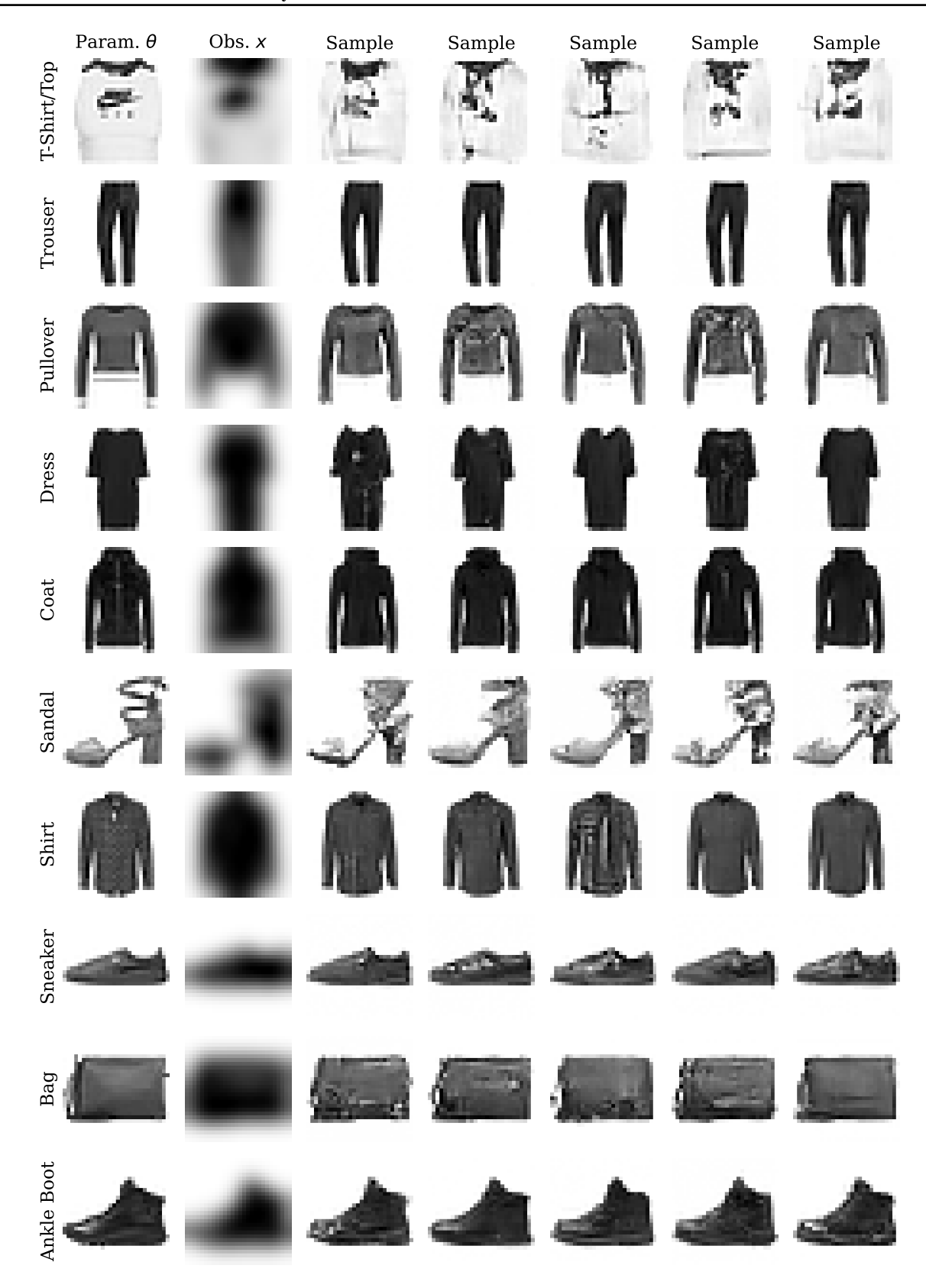


Figure 10: **FMPE - U-Net architecture - 60 000 training images**. FMPE denoising results from each class of Fashion MNIST obtained using a U-Net architecture. A large training set of 60 000 images was used.

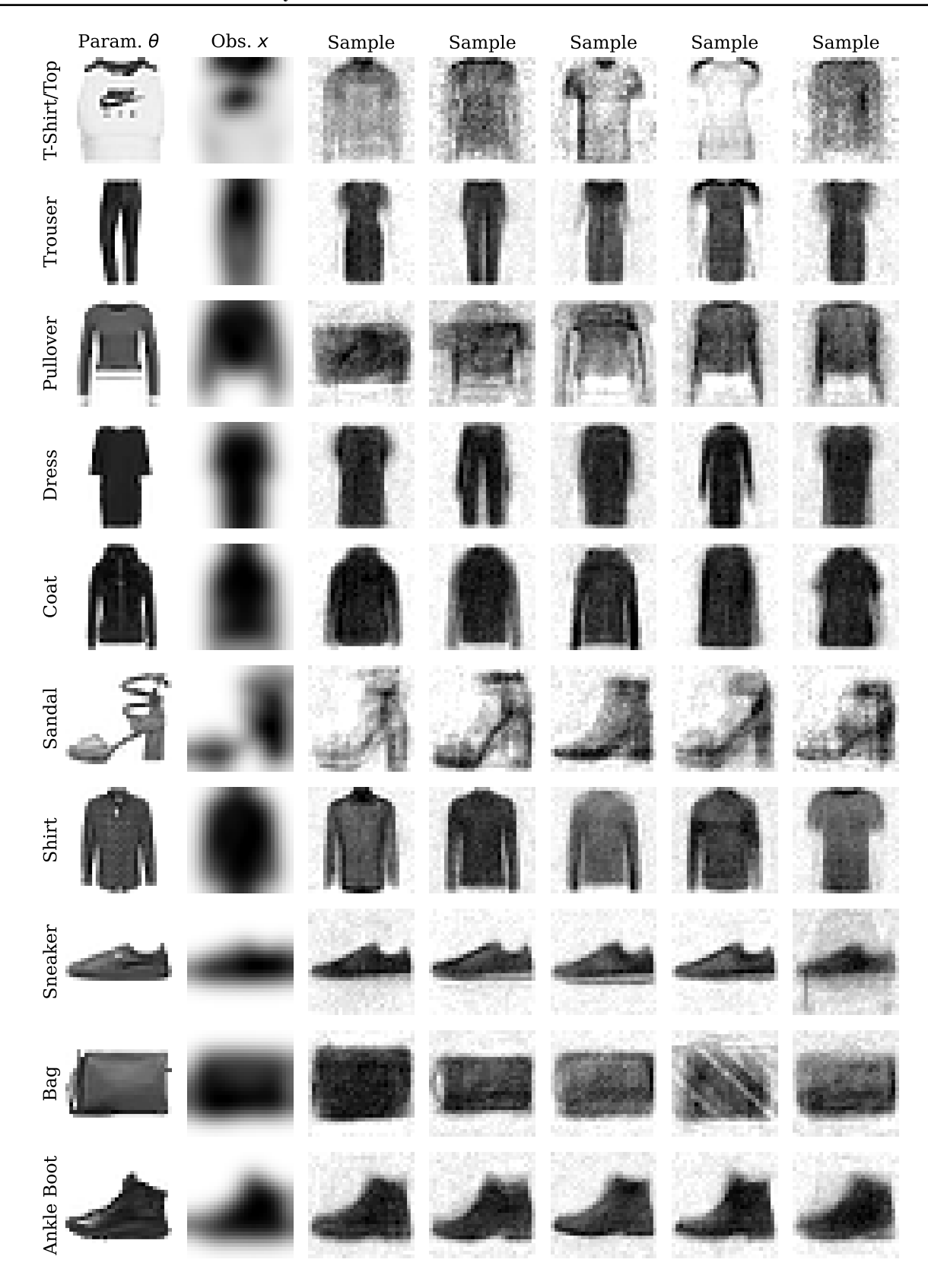


Figure 11: **CMPE - Naïve architecture - 2000 training images**. CMPE denoising results from each class of Fashion MNIST obtained using the naïve architecture described above and two-step sampling. A small training set of 2 000 images was used.

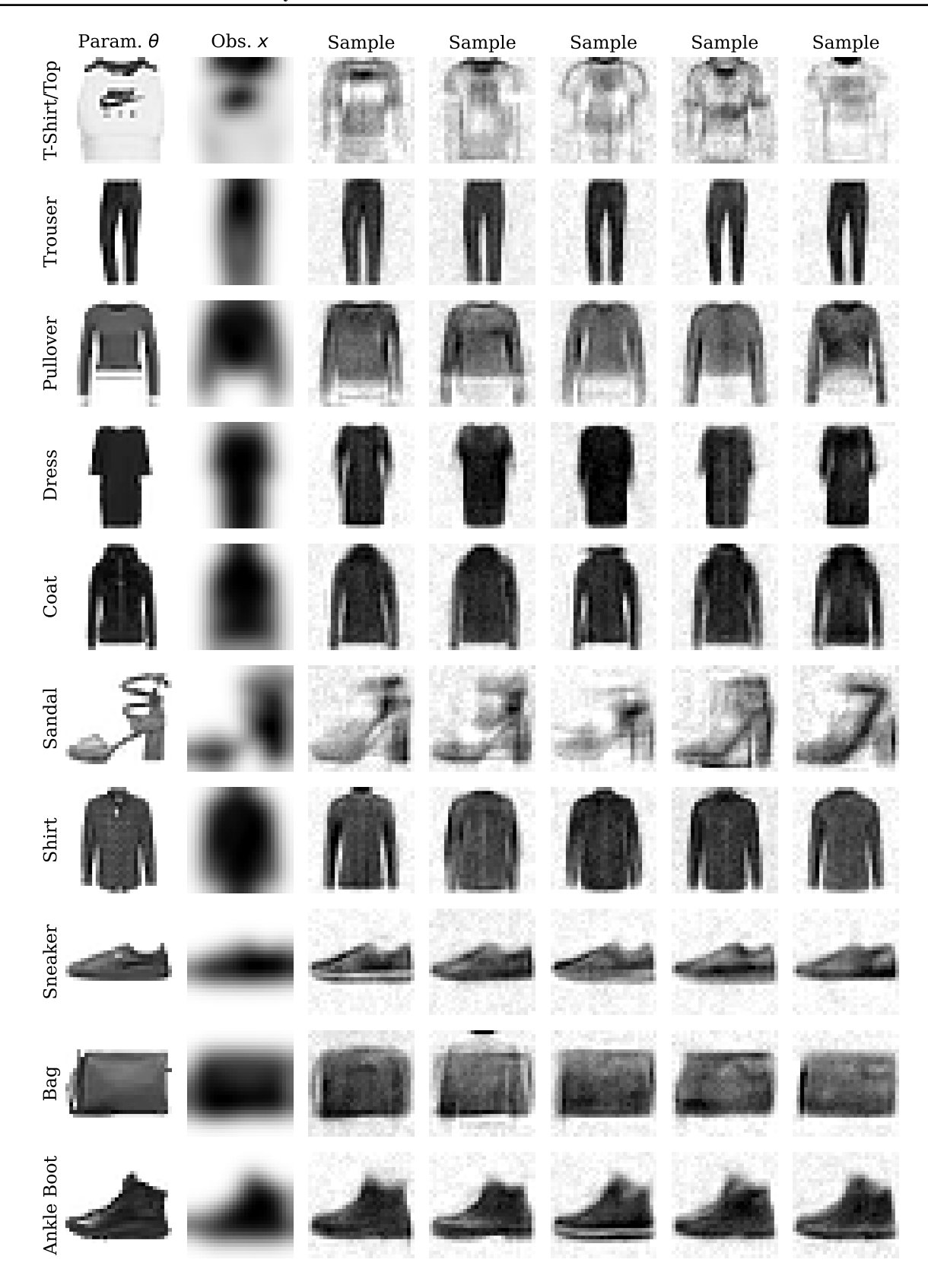


Figure 12: **CMPE - Naïve architecture - 60 000 training images**. CMPE denoising results from each class of Fashion MNIST obtained using the naïve architecture described above and two-step sampling. A large training set of 60 000 images was used.

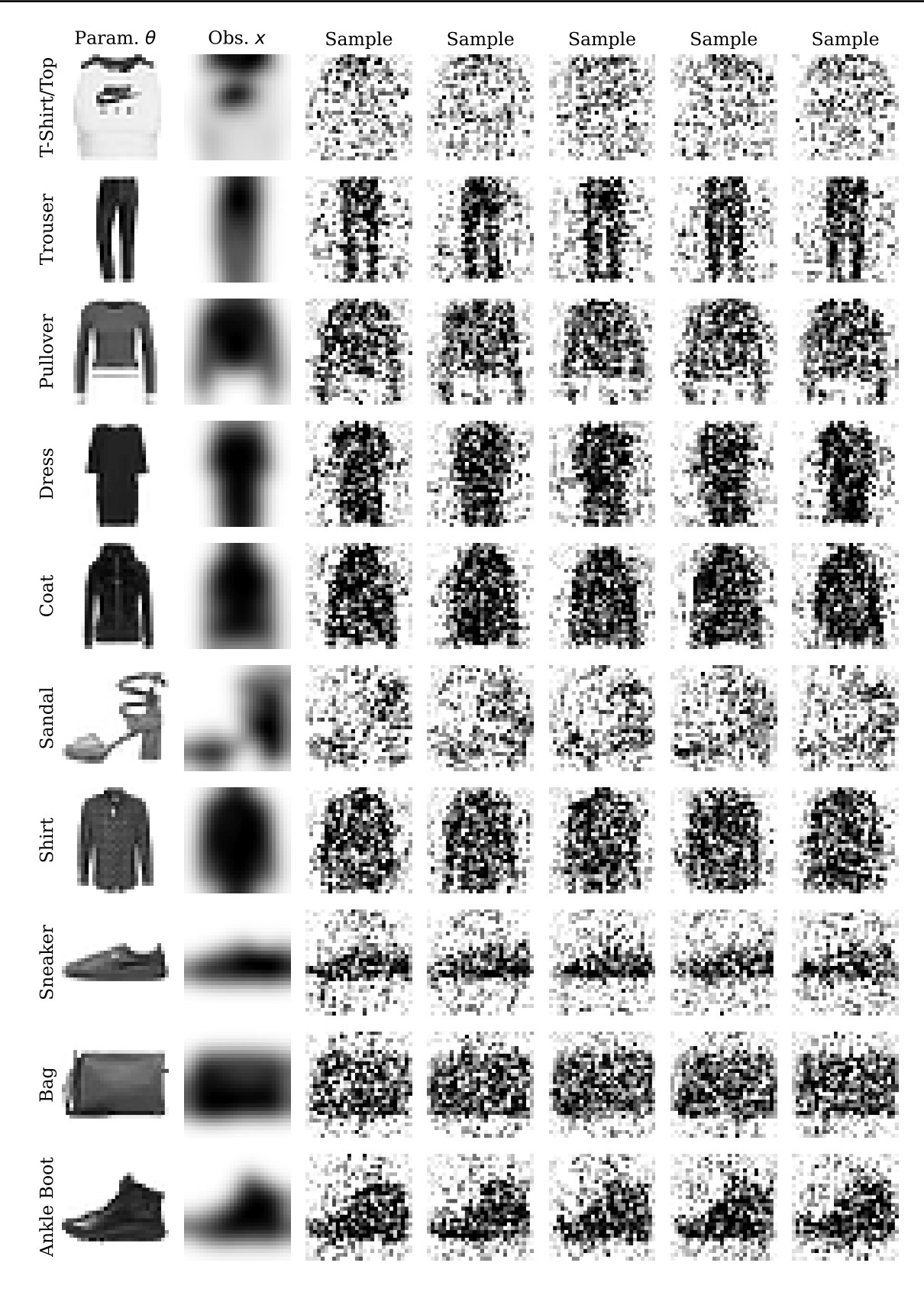


Figure 13: **FMPE - Naïve architecture - 2 000 training images**. FMPE denoising results from each class of Fashion MNIST obtained using the naïve architecture described above. A small training set of 2 000 images was used.

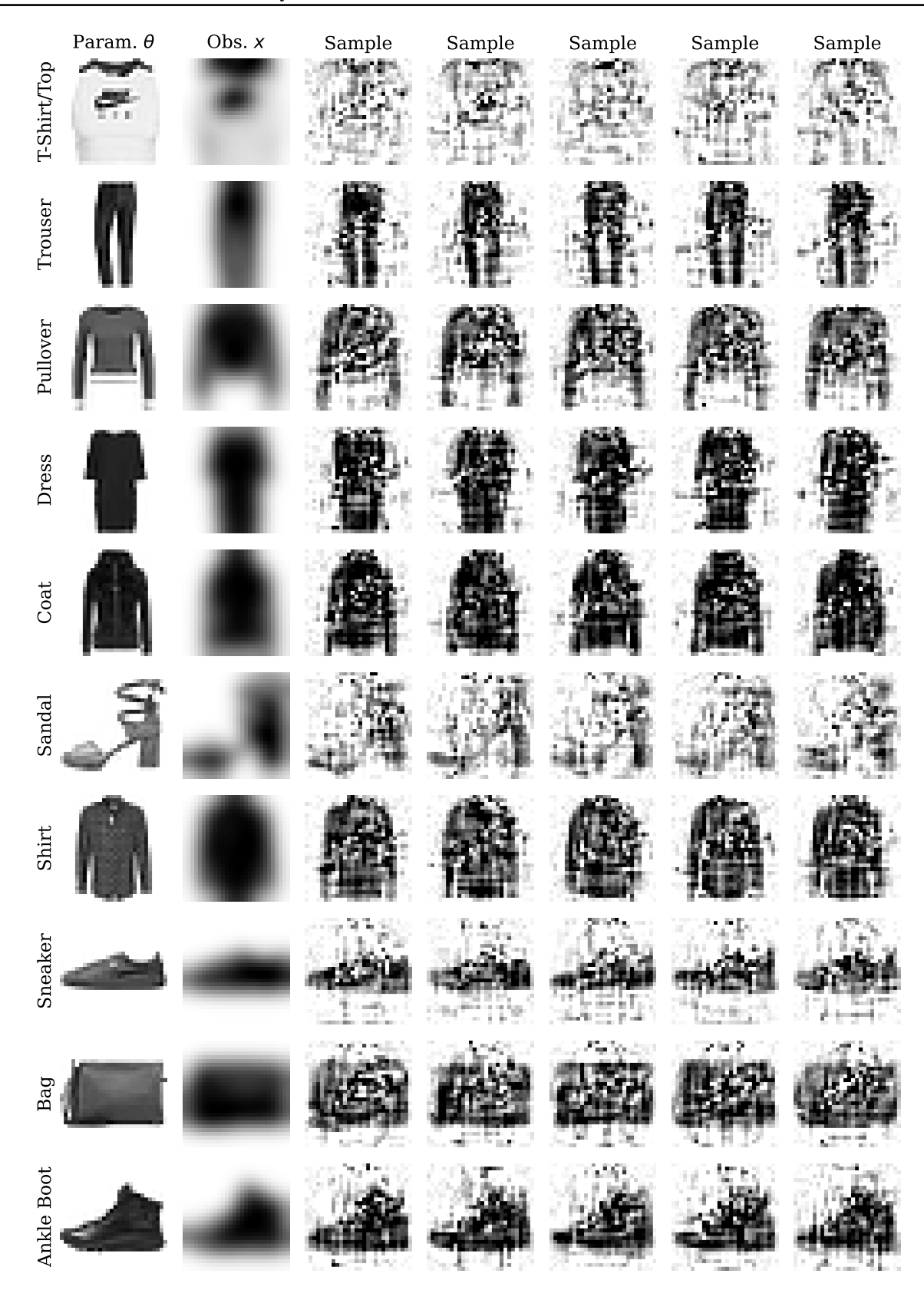


Figure 14: **FMPE - Naïve architecture - 60 000 training images**. CMPE denoising results from each class of Fashion MNIST obtained using the naïve architecture described above. A large training set of 60 000 images was used.